

30. Biomedical X-Ray Phase-Contrast Imaging and Tomography

Han Wen

This chapter reviews the main categories of methods that have been developed for preclinical and clinical imaging applications. The methods covered here are all based on geometric magnification by the projection of a cone beam emitted from a pseudopoint source, without the use of a lens or other types of focusing optics. These methods share the common goal of detecting x-ray refraction and diffraction, in order to complement the conventional attenuation contrast information in radiography and computed tomography.

30.1	Overview	1451
30.2	In-Line Phase-Contrast or Free-Space Propagation-Based Method	1453
30.3	Wavefront Tagging	1455
30.4	Wavefront Tagging with Grating Interferometry	1456
30.5	Diffraction-Enhanced Imaging with Monolithic Crystal Collimator and Analyzer	1460
30.6	Split-Beam Interferometry	1461
30.7	Conclusion	1463
	References	1463

30.1 Overview

In this chapter the phrase *phase-contrast imaging* refers to two- or three-dimensional (3-D) imaging techniques that are sensitive to the wave aspects of x-rays. This chapter considers imaging techniques that do not use magnifying optics. Methods involving magnifying optics, such as zone plates and curved mirrors, are discussed in other chapters. Among various forms of x-ray imaging, full-field imaging in physical space will be discussed, while reciprocal space methods such as coherent diffraction imaging and raster-scanning-based methods are outside the scope.

As an electromagnetic wave, the wavefront of an x-ray beam is the surface in three-dimensional space that has the same phase of wave oscillation, or the isophase surface. X-rays primarily interact with electrons in matter. In the classical picture, elastic scattering of an x-ray wave by atoms and molecules produces outgoing waves in an angular distribution. Elastic scattering means that the frequency of the wave oscillation is unchanged. Scattered waves in the forward direction give rise to a collective effect, which is a change of the speed at which the wave front travels (the wave vector). This effect is characterized by the real part of the index of refraction of the material.

Elastic scattering outside the forward direction results in a divergence of the wave propagation direction. Depending on the scattering angle, it is referred to as wide-angle x-ray scattering (WAXS), small-angle x-ray scattering (SAXS), and ultrasmall angle x-ray scattering (USAXS). In the rest of the chapter, the word *scattering* refers to the divergence of the wave propagation direction due to elastic scattering with microscopically heterogeneous structures down to the molecular level. It is worth noting that the angle of elastic scattering can be wide enough for the scattered x-rays to miss the detector of an imaging system, which leads to a perceived *attenuation* of the x-ray beam, even though no energy is deposited in the medium. This effect is distinct from the inelastic processes such as Compton scattering and the photoelectric effect, which deposits energy into the medium.

As is well known in optics, x-ray waves undergo refraction when encountering spatial variations of the index of refraction. Refraction is a change of the direction of propagation when the wave passes through a transition between two regions of different refractive index. A special type of refraction is a deflection of the wave by a sharp transition of the refractive index across

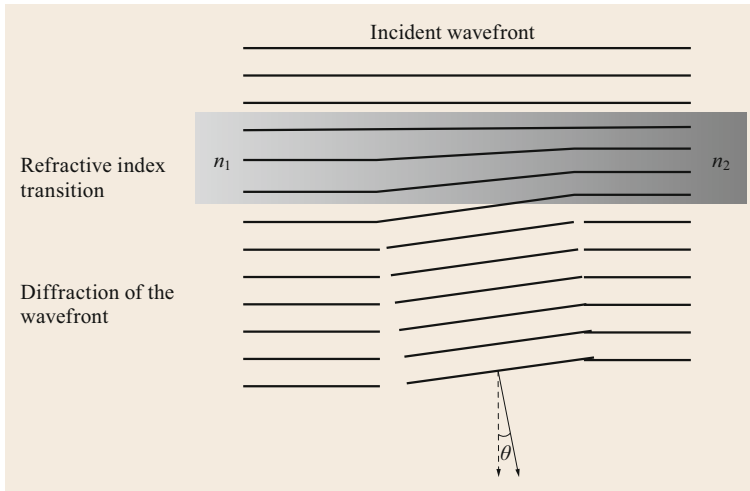


Fig. 30.1 Diffraction of an x-ray wave by a sharp transition of the index of refraction across the wavefront. The deflection angle θ is the change of the wave propagation direction through the transition zone

the wave front, such as the edge or corner of an object (Fig. 30.1). This is referred to as *diffraction*.

Current x-ray detectors only measure the intensity of an x-ray beam, which can be in the form of the integrated energy of the incident beam or the number of photons. X-ray phase-contrast imaging techniques either directly or indirectly sense wave refraction through mechanisms that convert it to an intensity signal. Most phase-contrast techniques can also detect and quantify x-ray scattering to various degrees.

The ability to detect variations of the refractive index and wave scattering adds new dimensions to the contrast-space of x-ray imaging and tomography. Conventional techniques share a common contrast mechanism, which is the attenuation of the x-ray beam. The image signal provides measurements in a two-dimensional (2-D) contrast space, which is attenuation

versus photon energy (Fig. 30.2). X-ray phase-contrast imaging adds the dimensions of bulk refractive index and wave scattering. In the context of biological and medical applications, a question is whether the refractive index is an independent contrast from attenuation. The answer lies in the x-ray properties of the constituent elements of biological materials with sufficient amount to be relevant for x-ray imaging. These elements are H, C, N, O, Ca and I, where iodine is a common extrinsic contrast-enhancing agent.

Consider a single-element material with a linear attenuation coefficient μ . An attenuation cross-section per electron can be defined as μ/ρ_e , where ρ_e is

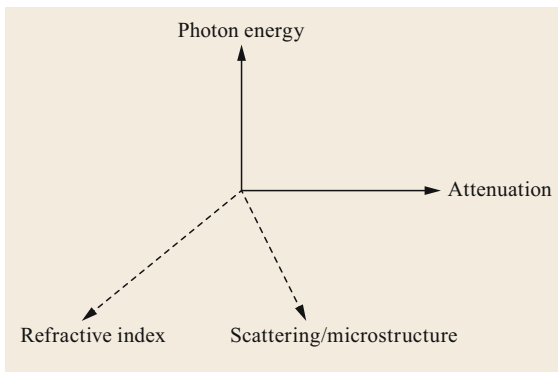


Fig. 30.2 In the contrast space of x-ray imaging, phase-contrast methods add the dimensions of refractive index and scattering to the conventional contrast of attenuation versus photon energy. Scattering as defined in the text is coherent scattering by microscopic heterogeneities

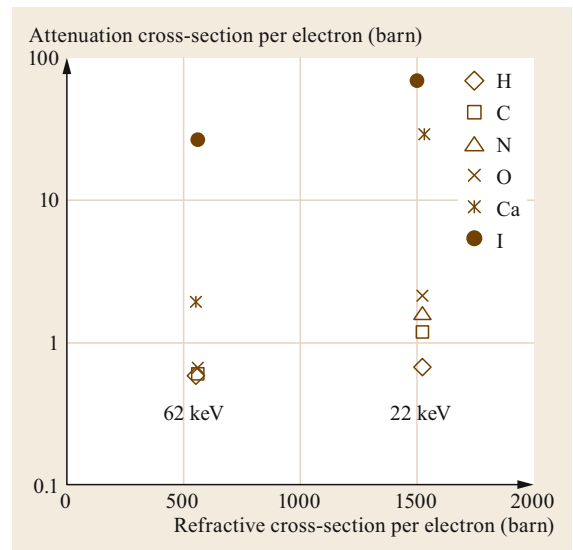


Fig. 30.3 Attenuation versus refractive phase shift per electron for the primary elements relevant to biomedical applications of x-ray phase-contrast imaging

the electron density. Similarly, if the material incurs a phase shift per unit length of φ on the wavefront, a phase shift, or refractive, cross-section per electron can be defined as φ/ρ_e . The attenuation and refractive cross-sections per electron for the elements H, C, N, O, Ca and I are readily calculated from reference tables [30.1]. They are plotted for two photon energies (Fig. 30.3). Since the refractive cross-section per electron is uniform across the elements, the refractive index measures the electron density regardless of the element. The attenuation cross-sections of the low-atomic number elements of H, C, N and O tend converge at higher photon energies, while calcium and iodine are more absorptive than the lower- Z elements. When considered together, it can be said

that the refractive index and attenuation provide independent information for the photon energy range of 20–100 keV.

Although wave scattering can be viewed as the consequence of a microscopic distribution of the refractive index in the Rayleigh scattering framework, it reveals unresolved heterogeneity in the material, which is an independent piece of information. Here, *unresolved* means length scales below the resolution of the imaging system.

In the rest of the chapter, several categories of x-ray phase-contrast imaging methods will be introduced. The description aims to help the reader grasp the principle of each type of technique rather than provide an exhaustive review of the literature.

30.2 In-Line Phase-Contrast or Free-Space Propagation-Based Method

This method relies on the diffraction of an x-ray wave to detect a sharp edge in the index of refraction [30.2–5]. When a wave encounters a sharp change of the refractive index in a direction across its front, it propagates at different speeds on the two sides of the boundary, resulting in a local deflection of the wave (Fig. 30.1). At a distance down beam, wave deflection redistributes the beam intensity, resulting in an intensity oscillation at the projected location of the edge, which can be observed with an imaging detector. Although the name *in-line phase-contrast* was initially given to this method [30.4], the name *free-space propagation* is also used since no optics are added to the beam path.

The diffraction-driven intensity oscillation is approximately proportional to the second derivative of the refractive index transition (slope of the slope), and thus has a bipolar shape [30.3]. In appearance it resembles a pair of adjacent bright and dark fringes, where the intensity in the dark fringe is displaced into the bright fringe. The polarity of the fringes is determined by the direction of the refractive index gradient and independent of the wavelength. Therefore, a polychromatic x-ray source is capable of creating this effect. Since the diffraction fringes enhance the visibility of the edge, the effect is often referred to as edge-enhancement.

In propagation-based methods the detector should have sufficient resolution to resolve the diffraction fringes. In the case of a parallel beam illuminating an infinitely sharp edge, the width of the diffraction fringes, defined as the distance between the valley and the peak of the bipolar fringe pattern, is on the order of $\sqrt{Z\lambda}$ for a propagation distance Z . The x-ray detector's resolution should be smaller than this width.

When a compact x-ray source such as an x-ray tube is used for illumination, the wavefront becomes a spherical surface and the geometry is called a cone beam geometry. For propagation-based phase-contrast imaging, the width of diffraction fringes of a sharp edge is $M\sqrt{Z_{\text{eff}}\lambda}$, where $Z_{\text{eff}} = R_1R_2/(R_1 + R_2)$ is the effective propagation distance from the object to the detector [30.4], R_1 and R_2 are the distances from the point source to the object and from the object to the detector, respectively, and M is the cone beam projection magnification factor of the object given by $M = 1 + R_2/R_1$.

Practically, compact sources are not point sources, but a finite area that emits x-rays. The size of the source area (focal spot in x-ray tube terminology), d , is an important parameter for propagation-based phase-contrast imaging. Its implication can be understood by treating the source as an integral of independent point sources that are distributed over the area. From a sharp edge in the object the point sources produce their individual diffraction fringes on the image plane. The individual fringes spread over the penumbra of the source on the image plane. The size of the source penumbra is dR_2/R_1 . The overall edge enhancement comes from the summation of the fringes. The amplitude of the sum is dependent on the ratio of the penumbra size over the fringe width

$$\frac{\frac{dR_2}{R_1}}{M\sqrt{Z_{\text{eff}}\lambda}} = \frac{d}{\sqrt{R_1\left(1 + \frac{R_1}{R_2}\right)\lambda}}$$

Higher ratios reduce the amplitude of the summation. That being the case, enhancement of sharp edges is often seen at a ratio of 2 or higher. It is therefore practical to retain edge enhancement in compact and

high-magnification setups with a short R_1 distance and commercially available microfocus x-ray sources.

For microtomography with microfocus sources, sufficient magnification allows efficient photon counting detectors to be used to provide $< 10 \mu\text{m}$ resolution in scan times of about 1 h [30.6]. Recognizing that the size of the source spot is the ultimate limit of spatial resolution, liquid-metal-jet anode x-ray tubes have been developed to reduce the spot size while maintaining the photon output [30.7]. Although the technology is still improving, in propagation-based phase-contrast tomography such sources provided better than $5 \mu\text{m}$ spatial resolution [30.8, 9].

On the other hand, although the parallel beams of synchrotron facilities do not provide a geometric magnification, their extremely high brightness allows high-resolution x-ray detectors with μm to sub- μm resolution. These detectors couple a visible-light microscope to a thin layer of scintillator crystal to achieve high spatial resolution. Propagation-based phase-contrast tomography at third-generation synchrotron sources, such as the advanced photon source of the Argonne National Laboratory, USA, can acquire an entire 3-D volumetric dataset in a second owing to the brightness of the beam and the short exposure time needed for each projection shot (<https://www1.aps.anl.gov/imaging>).

For tomographic reconstruction, although the edge-enhanced projection images can be fed directly into standard algorithms designed for attenuation contrast images, the question of how to extract quantitative information about the refractive index distribution is a topic of continued interest and development. A number of methods under various approximations, such as the paraxial approximation or the transport-of-intensity equation in the very near field, have been formulated to retrieve phase shift information from a single projection image, which are suitable for tomographic reconstruction [30.10, 11]. A method to retrieve both absorption and phase shift from a spectrally resolved detector has also been proposed [30.12]. A spectral detector can separate photons of different energies from a polychromatic source, thus providing multiple images of different photon energies in a single exposure.

Numerous uses of propagation-based x-ray phase-contrast imaging have been demonstrated, which would require an entire volume to describe. An example of biological application is the imaging of lung function. Diffraction by tissue-air interfaces in the lung parenchyma produces a field of intensity speckles in the projection image when illuminated with a sufficiently small source and observed with sufficient resolution. Figure 30.4 is such an example from Marcus Kitchen and Dylan O'Connell of Monash University. It is an image of a rabbit kitten thorax that has been inflation-fixed

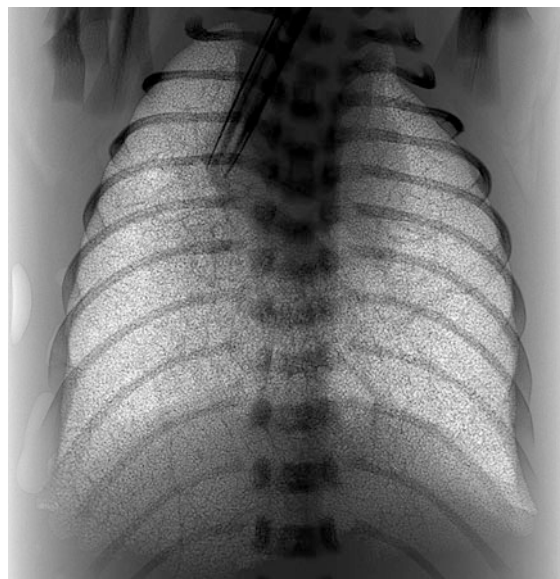


Fig. 30.4 An example of propagation-based phase contrast. This projection image of a rabbit kitten thorax, which has been inflation-fixed and embedded in agarose gel, was taken with a microfocus x-ray source. The speckle pattern in the lungs comes from the diffraction by the numerous air-tissue interfaces in the lung parenchyma over a sufficient wave propagation distance

and embedded in agarose gel. The image was recorded using a liquid-metal-jet micro-focus x-ray source [30.7] of approximately $20 \mu\text{m}$ focal spot size, with an exposure time of 15 s, source-to-object distance of 41.5 cm and geometric projection magnification factor of 7.95. Tracking the motion of the speckle pattern seen in such lung images provides information on tissue movement and function in the lung [30.13–17]. Another application is the visualization of air-filled blood vessels in organ specimens [30.18].

Clinical application of propagation-based phase-contrast imaging has also been realized for mammography in a commercial system (Konica Minolta Inc). It can be argued that propagation-based phase-contrast imaging is the most widely used phase-contrast technique today owing to its simplicity and convenience. It does not require additional hardware or scan time when compared to conventional x-ray imaging, the latter being an important factor for tomography. In terms of postprocessing there is a wide latitude of technical sophistication that the user can choose from depending on the level of quantification that is needed. For microscopy and microtomography in the laboratory setting, geometric magnification relaxes the requirement on detector resolution, and the demand for small source size is being met with improved x-ray tube designs.

30.3 Wavefront Tagging

This class of methods place one or more masking elements into the x-ray beam to introduce intensity tags in the projected x-ray image. Refractive bending of the x-rays by an object displaces the tags, while scattering of the x-rays blurs the contrast or visibility of the tags.

A simple and convenient method is to project an opaque grid onto the image plane, illustrated in Fig. 30.5 [30.19–22]. The shadows of the grid lines are the intensity tags on the wavefront. The idea of inserting a grid into a light beam appeared at least as early as 1900 as a way to check the quality of optics in astronomical telescopes [30.23]. In x-ray phase-contrast imaging, the object can be placed down beam from the grid. Projection of the object is superimposed over the grid shadows.

Wave refraction and diffraction in the object results in deflection of the x-rays from their original directions, which appear as a local movement or deformation of the grid shadows in the image. The movement of the grid shadows is proportional to the deflection angle of the x-rays, which is the slope of the wavefront in the direction perpendicular to the grid line. The amount of movement relative to the period of the grid can be rep-

resented as a phase shift, which is called the differential phase-contrast signal.

Additionally, x-ray scattering by nano- to microstructures in the object leads to a divergence of transmitted rays, which reduces the contrast or visibility of the grid shadows. The attenuation of grid contrast, therefore, provides a scattering image (Fig. 30.6). A reference shot without any object is usually taken to provide a reference for these measurements.

In a single exposure of the object, the displacement and blurring of the grid shadows can be measured with a harmonic analysis in the Fourier domain [30.19, 20], or by feature tracking in real space [30.21, 22]. If the grid shadows are below the resolution of the detector, a second grid can be inserted to create a broad moiré pattern with the first grid to allow detection [30.24].

Cross-grids are used to obtain two-dimensional vectors of the slope of the wavefront [30.25]. In an object of complex structures, vector analysis of the wavefront slope field provides landmarks for dynamic tracking of movement and flow [30.26].

Since the angular spread of x-ray scattering is on the order of λ/D , where D is the characteristic size of

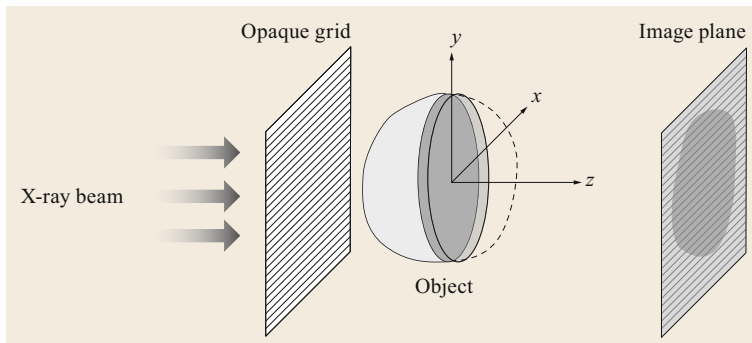


Fig. 30.5 Phase-contrast imaging with a single grid. Wavefront refraction and scattering appear as deformation and blurring of the projected grid lines

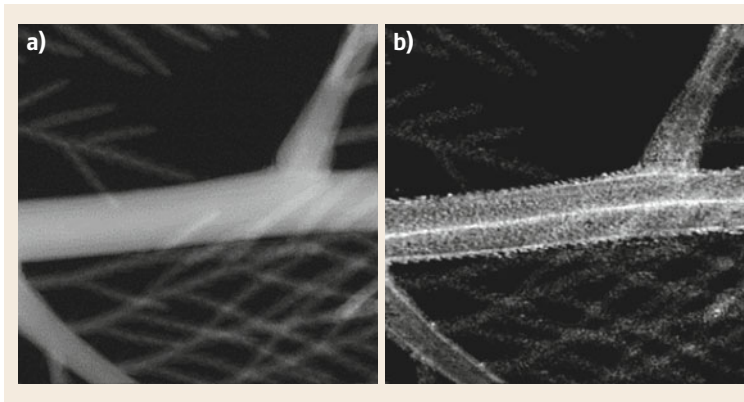


Fig. 30.6a,b A fir branch imaged in a benchtop x-ray phase-contrast system containing an opaque grid. From a single exposure, an attenuation image (a) and a scattering image (b) are obtained

the scattering structure, contrast reduction of the grid shadows depends on the size of the scatterers. Quantitatively, the level of contrast reduction relates to an autocorrelation of the complex refractive index distribution [30.19, 20, 27, 28]. The correlation length is determined by specifics of the imaging system, such as the grid density and the distance from the object to the detector, as well as the x-ray wavelength. The grid contrast reduction tends to increase with the size of the scattering structures up to the correlation length of the system, and then plateau or slightly decrease with larger scatterers. This property has been used to selectively image nanoparticles of a certain size while suppressing background signal in both radiography and tomography [30.28, 29].

In single-shot grid-based phase-contrast imaging, the resolution in the direction across the grid lines is generally limited to the period of the grid shadows. Higher resolution can be recovered through a phase-stepping process, which acquires multiple images while the position of the grid shadows is scanned incrementally [30.30]. A linear scan of sufficient resolution can decode a two-dimensional grid pattern [30.31].

The diffraction fringes of a knife edge are used as wavefront intensity tags in the edge illumination

method [30.32–34]. A masking edge can be placed in front of the detector to resolve the sharp boundaries of the Fresnel fringes, which are usually below the resolution of the detector.

Besides opaque grids, a phase grid that imprints a periodic phase pattern on the wavefront can also be used to create an intensity fringe pattern on the image plane through the Talbot self-imaging effect [30.35, 36], which serves as the intensity tags for wavefront measurements. Random absorptive and phase masks of sufficient feature density, such as sandpaper, can be used to project a dense speckle pattern on the image plane [30.37–40]. The movement and contrast of the speckle pattern can be quantified locally to provide wavefront slope and scattering measurements in the same way as regular grid lines.

Owing to its simplicity, speed and quantitative nature, wavefront tagging using grids, sandpapers etc. has seen diverse applications. The first imaging experiment in a live animal utilized an x-ray grid [30.41]. One example is the detection of nanoparticle-labeled hepatic cancer cells in mouse models using grid-based scatter imaging [30.42–45]. Another fruitful application is the imaging of airway surface liquid layers in animal models of respiratory disease and treatment [30.21, 22].

30.4 Wavefront Tagging with Grating Interferometry

For a grating of period P that is much larger than the x-ray wavelength λ , the near field of wave propagation is up to distances on the order of P^2/λ . In this range, the Talbot self-imaging effect of a grating is the appearance of intensity fringes at certain propagation distances [30.35, 46]. The Talbot images of x-ray phase gratings of micrometer periods provide wavefront tags that have been used extensively for phase-contrast imaging [30.47–51]. Like wavefront tagging with crossed grids described in the previous section, two-dimensional gratings or pairs of crossed linear gratings can be used to measure the 2-D vector of wavefront slopes [30.52–55].

In some instances, particularly with bright synchrotron sources, the Talbot fringes can be resolved directly with x-ray microscopes. In other instances where the fringes are below the detector resolution, an opaque (absorption) grating is placed over the Talbot fringes, which is called an analyzer grating (Fig. 30.7). The analyzer grating forms a broad intensity pattern with the Talbot fringes due to the classic moiré effect, which can then be resolved by the detector. The classic moiré effect is a beat pattern arising from two regular bright-and-dark patterns overlaid on top of each other.

An example is the overlay of two sets of dark lines of similar periods (Fig. 30.8). In addition to the magnifying effect, a small movement of the Talbot fringes is proportionally magnified as a similar movement of the moiré fringes, thus making it possible to measure small deflections of the x-rays.

In compact systems that use conventional x-ray tubes of a finite source area, the penumbra of the source on the image plane can blur the Talbot fringes and substantially reduce their contrast. To solve this problem, a second absorption grating can be placed in front of the source (Fig. 30.7) to act as a regular array of narrow slits. Each slit is sufficiently narrow to avoid fringe blurring by its penumbra. The wavefronts from individual slits are mutually incoherent, and thus their Talbot fringes sum in intensity in the image. By choosing the right period for the source grating, the Talbot fringes of neighboring slits sum constructively to provide an overall fringe pattern. The three-grating configuration including a source grating, a phase grating and an analyzer grating was proposed as the Talbot–Lau interferometer [30.48, 51]. The x-ray source grating can be replaced with a set of line sources in an x-ray tube containing a structured anode [30.56, 57]. Similarly, the

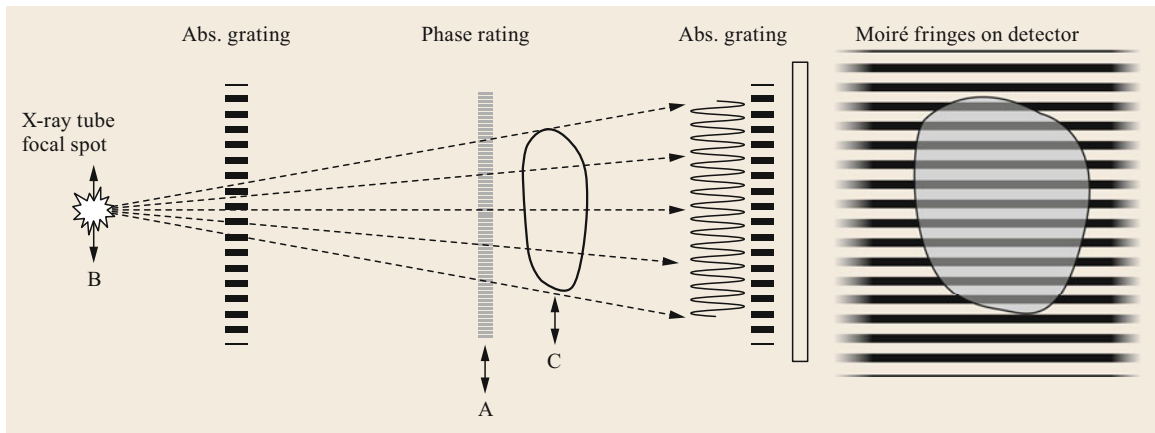


Fig. 30.7 Using a Talbot–Lau interferometer to produce and detect micron-scale intensity fringes on the wavefront. Different phase-stepping methods are used to measure fringe movement and fringe-contrast reduction. A. Phase stepping by moving one of the gratings. B. Electromagnetic phase stepping by steering the x-ray source spot with an electromagnetic field. C. Scanning the sample through the field of moiré fringes

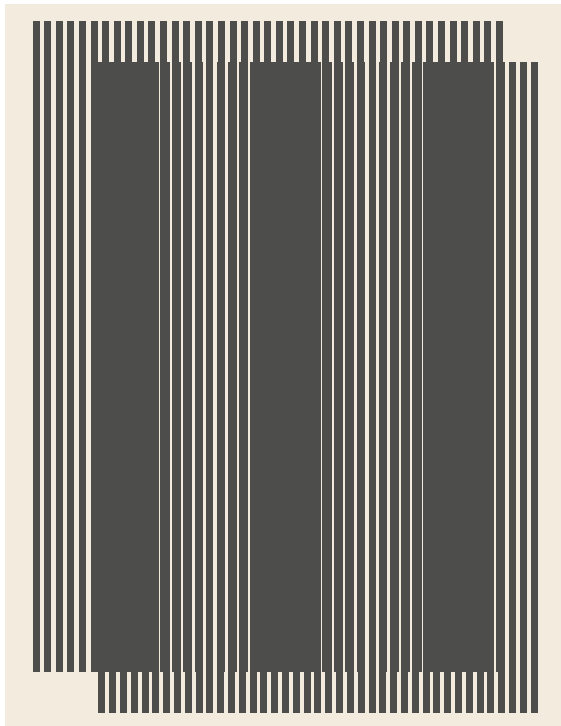


Fig. 30.8 The classic moiré pattern between two sets of intensity lines of similar periods

analyzer grating can be replaced with a structured x-ray scintillator in the detector consisting of interspersed lines of x-ray conversion material [30.58, 59].

Quantitative measurements of the displacement and contrast-reduction of the Talbot or moiré fringes can be made with single-image methods in the same fashion

as wavefront tagging with grids described previously. The analyzer grating can also be spatially modulated to create a fringe pattern in exact alignment with the detector pixel rows to facilitate single-image measurements [30.60]. Alternatively, phase stepping methods that involve multiple images can be used [30.30]. The idea of phase-stepping is to ensure that each physical point in the object experiences a complete cycle of the wavefront tags, such that the tag amplitude and position can be measured for each physical point.

Several methods of phase stepping have been devised for x-ray phase-contrast imaging, which are illustrated in Fig. 30.7. One is to physically scan the position of a grating in its plane in subperiod steps [30.30, 49, 50, 61, 62]. A second method without physical movement is to electromagnetically steer the x-ray source spot, causing relative displacement between the projection of the object and the fringe pattern [30.63]. A third method scans the fringes by a relative movement between the object and the imaging system [30.64, 65]. In tomographic scans, phase stepping can be distributed amongst the projection angles to reduce the total number of images that need to be acquired [30.62]. In practice the amount of phase shift in each step and the uniformity of the phase shift across the image often fluctuate and are unknown, for example due to instrument stability limits. An image-based algorithm can be used to find the phase shift and its global distribution of each image based on the movement of the fringes, thereby adaptively retrieving the wavefront slope and scattering information without knowing the phase shift a priori [30.63, 66].

The sensitivity of wavefront tagging methods to x-ray diffraction and scattering approximately scales

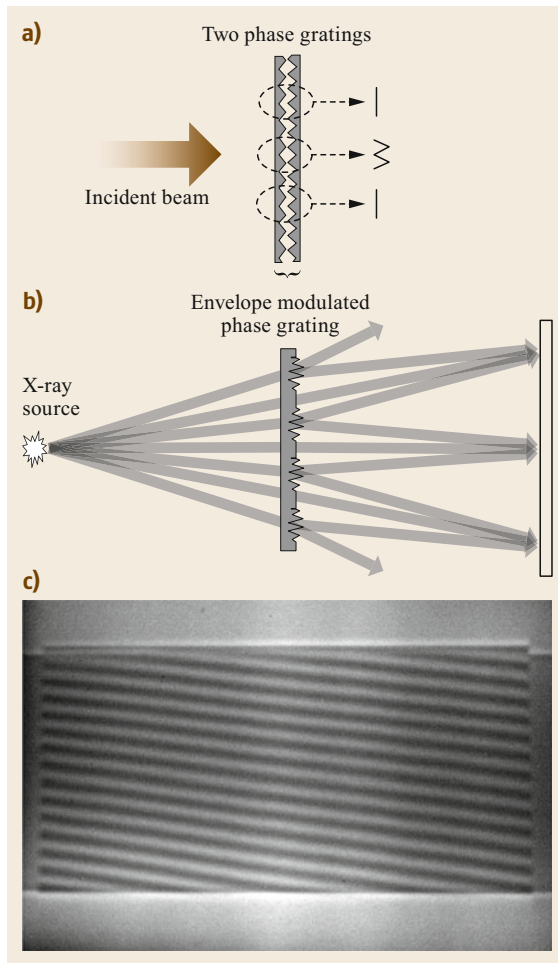


Fig. 30.9a–c The phase moiré effect between two sets of linear phase patterns of similar periods. **(a)** Two phase gratings of slightly different periods are overlaid facing each other. Their combined phase shift alternates between a constructive sum and a destructive cancellation. Effectively they function as a single phase grating of a broad envelope modulation. **(b)** The incident beam is strongly or weakly diffracted according to the envelope modulation. At sufficient distances down beam, the photon flux is redistributed into a moiré pattern. **(c)** The actual moiré pattern between two overlaid x-ray phase gratings of different periods is shown ◀

ings can increase the line density and effect path length through the gratings [30.67–70] but at a cost of reduced image area. The alternative multiline sources and detectors with structured scintillators are also limited in how small their features can be due to fabrication processes specific to the anode and scintillator materials.

In search of high sensitivity, a universal moiré effect was discovered that allowed wavefront tags in the form of regular phase patterns [30.71]. Since materials incur greater phase shift than intensity attenuation on hard x-rays, phase gratings are less than 1/10th the depth of intensity gratings and can be made to sub- μm periods [30.72].

The universal moiré effect encompasses the classical intensity moiré effect and a phase moiré effect as two ends of a continuous spectrum [30.71]. An example of the phase moiré effect is the overlay of a pair of phase gratings of slightly different periods (Fig. 30.9a). Their combined phase shift alternates between a constructive sum and a destructive cancellation (Fig. 30.9a). Effectively, they act as a single phase grating of a broad envelope modulation (Fig. 30.9b). The incident beam is diffracted strongly in some locations and weakly in others according to the envelope modulation (Fig. 30.8b), leading to a redistribution of the photon flux and intensity bands at a sufficient distance down beam. The width of the envelope modulation is at least several times the

with grating period/propagation distance, which motivates the drive to smaller gratings periods. However, intensity gratings require substantial path length through a dense material such as gold to block hard x-rays, which can require high-aspect-ratio structures that are difficult to make. Tilted gratings and reflective grat-

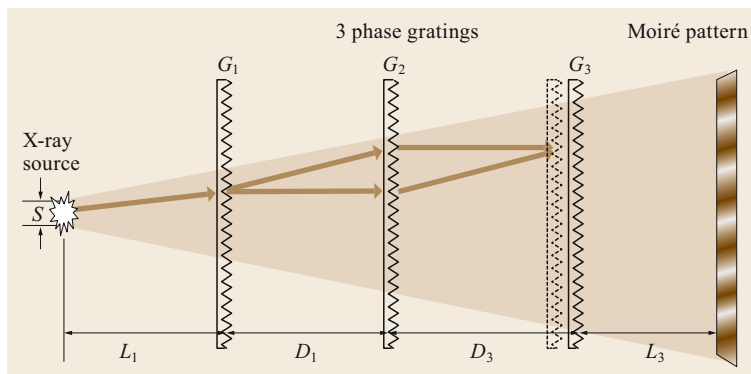


Fig. 30.10 A polychromatic far-field interferometer consisting of three phase gratings. The focusing effect of G_2 forms a series of achromatic Fourier images of G_1 as represented by the dotted outline. The grating G_3 creates a phase moiré effect with the Fourier images of G_1 , which casts a moiré fringe pattern further down beam at the image plane

grating period, and thus the moiré pattern appears much farther than P^2/λ (far field). An example of a moiré pattern between two overlaid x-ray phase gratings of 399 and 400 nm periods is shown in (Fig. 30.9c), which are illuminated by a tungsten-anode x-ray tube operating at 60 kVp. The phase moiré effect remains when there is a gap between the two phase gratings, as self-images of the first grating are projected onto the second grating at appropriate gap distances. Since the spatial frequency of the moiré bands equal the difference between the projected frequencies of the two gratings, the effect diminishes with large gaps between the two gratings when the bands become too dense to resolve.

Imaging systems consisting of only two phase gratings have been used to scan a continuous range of scattering length scales with both neutron and x-ray beams by varying the gap between the gratings [30.73, 74]. However, their phase sensitivity, determined by

grating period/intergrating gap, is limited by the small gap spacing. The limitation is overcome in a method consisting of three phase gratings, called a polychromatic far-field interferometer (PFI) (Fig. 30.10). Here the middle grating forms a series of Fourier images of the first grating on or near the plane of the third grating [30.75]. The Fourier images produce a phase moiré effect with the third grating. The intergrating spacings are now unlimited, and ultrahigh sensitivity phase-contrast imaging at fractions of clinical dose levels have been shown in tissue specimens and mammography phantoms, using sub- μm period phase gratings operating in the far field and the hard x-ray regime [30.71, 76]. Figure 30.11 is an example that compares radiographs of a formalin-fixed mouse pup specimen taken with a PFI system (Fig. 30.11a,b) with conventional attenuation radiography taken with a clinical digital mammography scanner (GE senographe essential) (Fig. 30.11c).

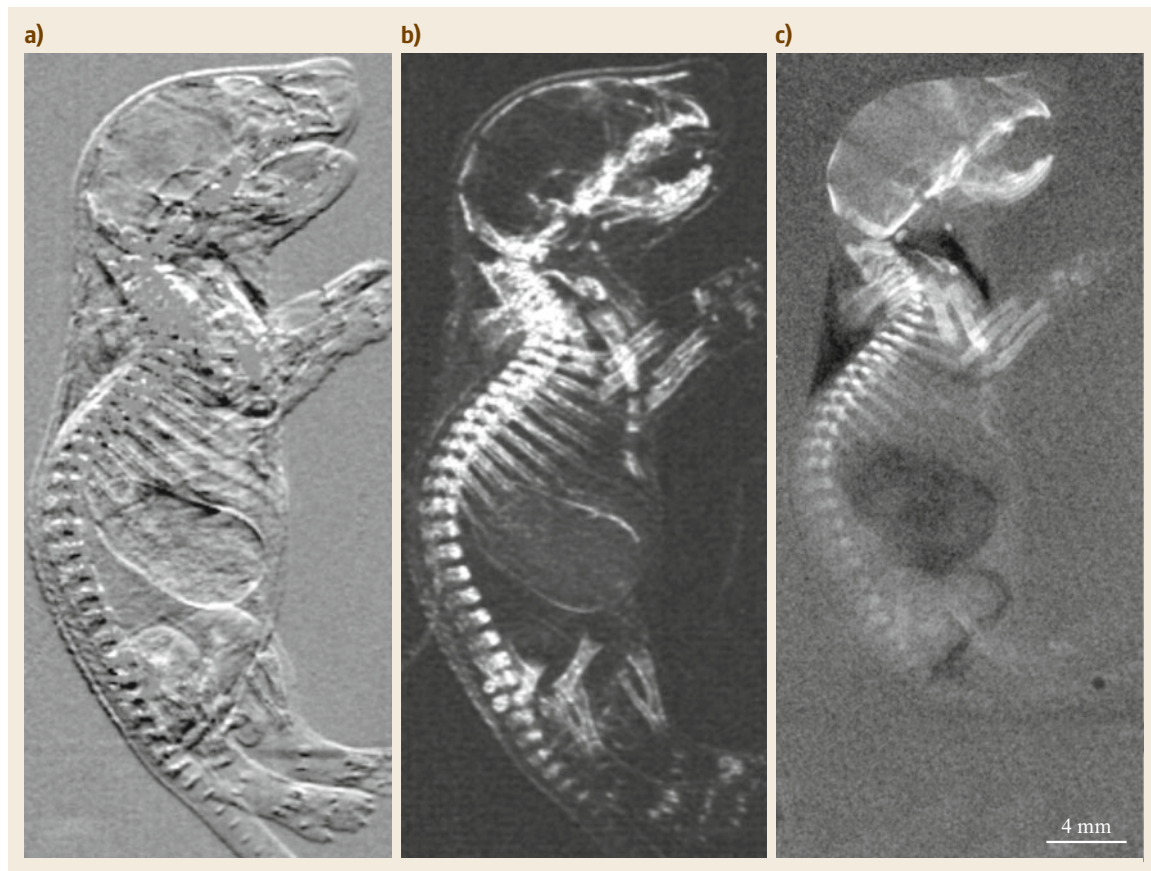


Fig. 30.11a–c A comparison of phase-contrast radiography with a PFI system and conventional radiography with a clinical mammography scanner. The sample is a mouse pup specimen. The exposure dose of the PFI scan was one-third that of the conventional radiography scan. A single PFI scan yields a differential phase-contrast image (a) and a scattering image (b). The differential phase-contrast image (a) reveals soft tissue structures that are invisible in the conventional attenuation-contrast radiograph (c)

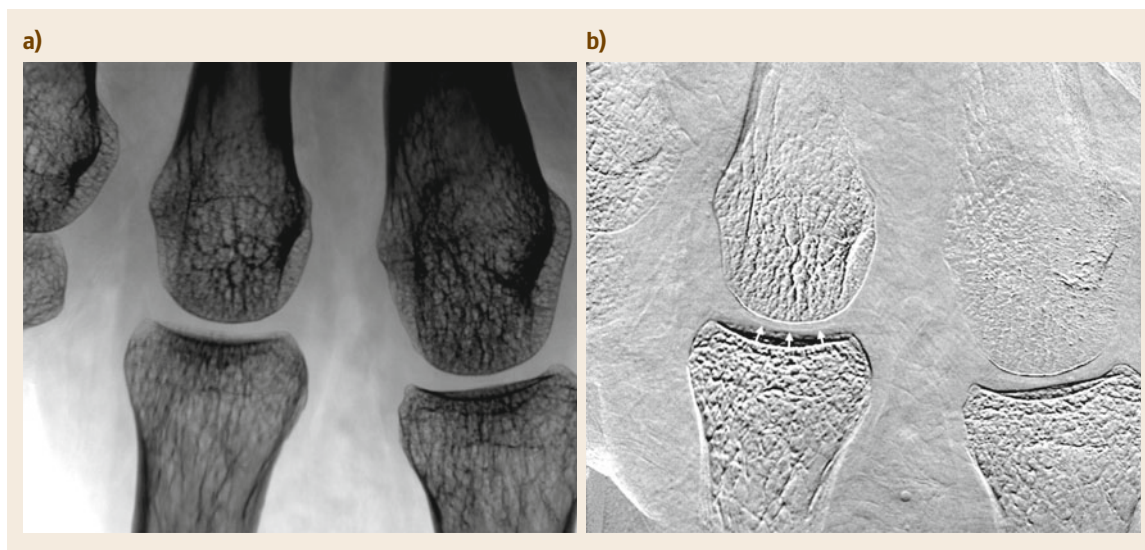


Fig. 30.12a,b The absorption (a) and differential phase-contrast (b) images of part of a volunteer's hand from a clinical grating-based phase-contrast radiography system. The metacarpophalangeal joints of the first and second fingers are in the field of view, and the smooth surface of cartilage is clearly depicted in the differential phase image as indicated by the arrows

The PFI system consisted of three phase gratings of 399, 400 and 400 nm periods [30.71]. Although the radiation dose of the PFI scan was one-third that of the conventional radiography, it revealed a substantial number of soft tissue structures that were absent in the conventional radiograph.

The numerous application-specific developments of grating interferometry will not be listed here. A few examples that point out the potential of these methods include brain specimen imaging [30.77], mouse fetus anatomical imaging [30.69], breast specimen

imaging [30.78–81], lung imaging [30.63, 82–84], nondestructive testing [30.85], food imaging [30.86] and plasma diagnosis in high-energy-density research [30.87]. Microtomography using a rotating Talbot–Lau interferometer has been implemented in a commercial system [30.88]. A clinical application of Talbot–Lau interferometry has also been realized by Momose et al. as a medical radiography system (Konica Minolta Medical and Graphic, Inc.) [30.89]. Figure 30.12 shows superior visualization of the cartilage in finger joints by the differential phase-contrast signal.

30.5 Diffraction-Enhanced Imaging with Monolithic Crystal Collimator and Analyzer

In its simplest form, an x-ray beam is first collimated through Bragg reflection on the surface of a monolithic crystal (Fig. 30.13). The collimated beam penetrates through an object before once again being reflected on the surface of a second, analyzer crystal [30.90–93].

Bragg reflection on the surface of a single crystal is restricted by the Bragg condition, which curtails the angular divergence of the x-ray beam to microradians [30.94]. The collimated beam undergoes diffraction and scattering when passing through the imaged object. As a result the transmitted beam can be deflected by a small angle and have a wider divergence. Further down beam, the second Bragg reflection by the ana-

lyzer crystal serves as an angle-sensitive detection of the transmitted beam. In the special case where the two crystals are identical and parallel to each other, diffraction and scattering in the object reduce the flux that reaches the detector.

A central concept of this method is the rocking curve, which is the double-reflected intensity as a function of the alignment angle between the two crystals. In the absence of an object in the beam, the curve peaks at the position where the Bragg condition is satisfied for both crystals. When an object is present, diffraction and scattering in the object result in shifting and broadening of the rocking curve, respectively. Although a full

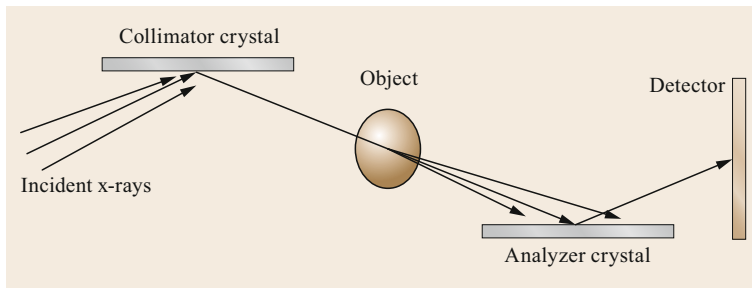


Fig. 30.13 Diffraction imaging with a single-crystal beam collimator and a single-crystal analyzer

measurement of the rocking curve provides complete information, it is sufficient in practice to acquire images at either one or several points on the rocking curve to quantify x-ray diffraction or scattering, or both [30.95–98]. The high sensitivity of this method, typically on the order of a microradian or better, is brought about by the selectiveness of the Bragg condition [30.99]. Unlike the wavefront-tagging methods mentioned in the previous section, the rocking curve is a direct measure of the angular distribution of x-ray scattering.

In Bragg reflection the angle of the outgoing beam is not simply equal to that of the incident beam. It is dependent on the crystal lattice structure and orientation, and the x-ray wavelength in addition to the incident angle. By an appropriate choice of these parameters, the reflected beam can be at a less acute angle from the surface of the crystal when compared to the incident beam,

giving an expansion of the beam size to cover a larger field of view for imaging [30.90].

Diffraction-enhanced imaging has been demonstrated in a number of biological applications owing to its sensitivity. Examples include breast imaging [30.93, 100–104] and musculoskeletal imaging [30.105–108]. X-rays are diffracted by the numerous microscopic air-tissue interfaces in the lung parenchyma leading to a divergence of the rays and a broadening of the rocking curve. This effect was first observed with diffraction-enhanced imaging and proposed as a way to evaluate parenchymal lung disease [30.92, 109]. An application in bioengineering is the visualization of low-density biomaterial in tissue engineering [30.110, 111]. Owing to its high sensitivity the stability in the alignment of the crystals is important, which has been addressed in table-top systems using conventional x-ray tubes [30.97].

30.6 Split-Beam Interferometry

The earliest x-ray interferometer is arguably the Bonse–Hart interferometer [30.112, 113], a classic split-beam interferometer where a beam is amplitude divided into two mutually coherent beams that travel distinct paths before merging to interfere with each other (Fig. 30.14). This is the most sensitive phase-contrast imaging method to date, providing an absolute phase shift measurement between the object and a reference beam. Unlike the visible-light Mach–Zehnder interferometer, which uses half-mirrors to split a beam [30.114], monolithic silicon crystals are used. A monochromatic x-ray beam is divided into two mutually coherent beams by a single crystal when the incident angle meets the Laue diffraction condition. Laue diffraction through three aligned crystals form two mutually coherent light paths of the same length. Residual strain or imperfections in the crystals result in a spatial distribution of phase difference between the two beams as they sum coherently in amplitude on the image plane, creating an intensity pattern that reflects constructive and destructive interference. Since the diffraction angle is approximately the

ratio of wavelength over the crystal lattice spacing, it remains large for hard x-rays resulting in widely separated light paths. When an object is introduced into one of the two paths, the interference pattern is altered by the additional phase shift incurred by the object. With phase stepping and phase unwrapping, a point-by-point measurement of the absolute phase shift map of the object is obtained [30.115–118]. Unlike the wavefront slope measurement by tagging or diffraction-enhanced imaging, this approach directly obtains the topography of the wavefront, which is unique among all methods. In practice the entire interferometer is often carved out of a single crystal to ensure perfect alignment and stability of the interferometer. Such an interferometers with a synchrotron sources remains the most sensitive phase-contrast imaging method today with the capability of providing accurate refractive index distribution in 3-D [30.119].

However, the extreme sensitivity of the crystal interferometer towards alignment and mechanical stability made it challenging to implement. Since optical phase

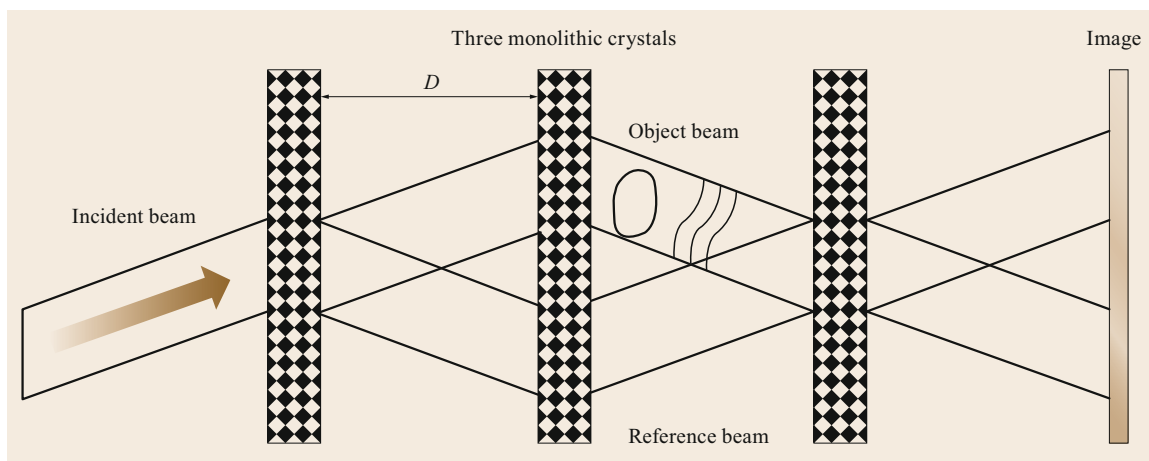


Fig. 30.14 The Bonse–Hart interferometer consists of three perfectly aligned monolithic crystals. The crystals are usually parts of a single block of silicon. Each crystal splits the monochromatic beam by Laue diffraction. The intercrystal spacing D is large enough that the object beam is completely separated from the reference beam. The interference pattern between the two provides an absolute phase shift measurement of the object

gratings are also effective beam splitters, an intermediate solution is to replace the first two crystals with gratings and use the last crystal as an analyzer, resulting in a grating shear interferometer [30.120]. Due to the use of the analyzer crystal, a monochromatic and collimated beam is needed. A further development is the grating–Bonse–Hart interferometer [30.121, 122], which replaces all three crystals with phase gratings of nanometric periods (Fig. 30.15). A beam of moderate bandwidth and angular divergence can be used. Small grating periods produce sufficiently large diffraction angles and separation of the light paths when a slit is used to limit the height of the incident beam. Typically, multiple pairs of mutually coherent light paths are generated and give rise to bands of interference fringes on the image plane. If an object intersects one

of a pair of interfering beams, the situation is the same as the Bonse–Hart interferometer and an absolute phase shift measurement is obtained. If the object intersects both beams, image twinning occurs and the measured phase shift is the difference between two locations in the object. Figure 30.16 is an example that compares the differential phase-contrast signals of a grating–Bonse–Hart interferometer and a Talbot–Lau interferometer in radiography of a formalin-fixed mouse kidney specimen [30.121]. The grating–Bonse–Hart interferometer was based on three phase gratings of 200 nm periods, while the Talbot–Lau interferometer included a combination of phase and absorption gratings of 4.8 μm periods. The order-of-magnitude difference in the grating periods resulted in a proportional amplification of the differential phase-contrast signal.

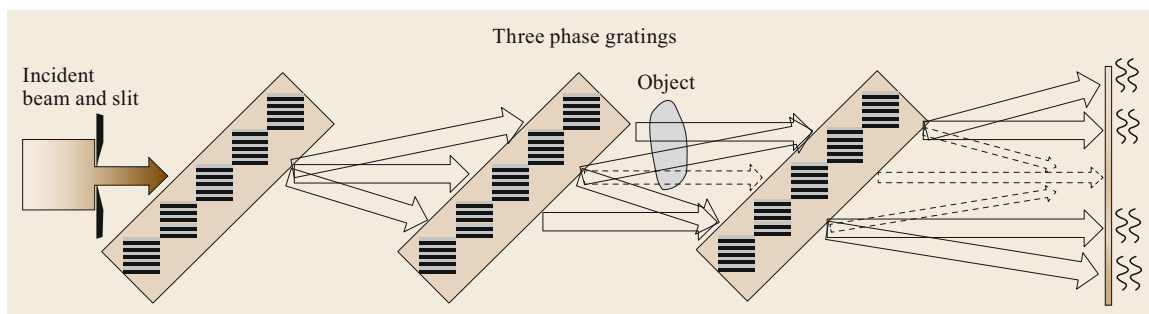


Fig. 30.15 A grating–Bonse–Hart interferometer consisting of three phase gratings. The incident beam is restricted in height by a slit and diffracted into multiple pairs of mutually coherent beams that produce bands of interference fringes on the image plane. The fringe pattern is achromatic, therefore allowing a polychromatic source to be used

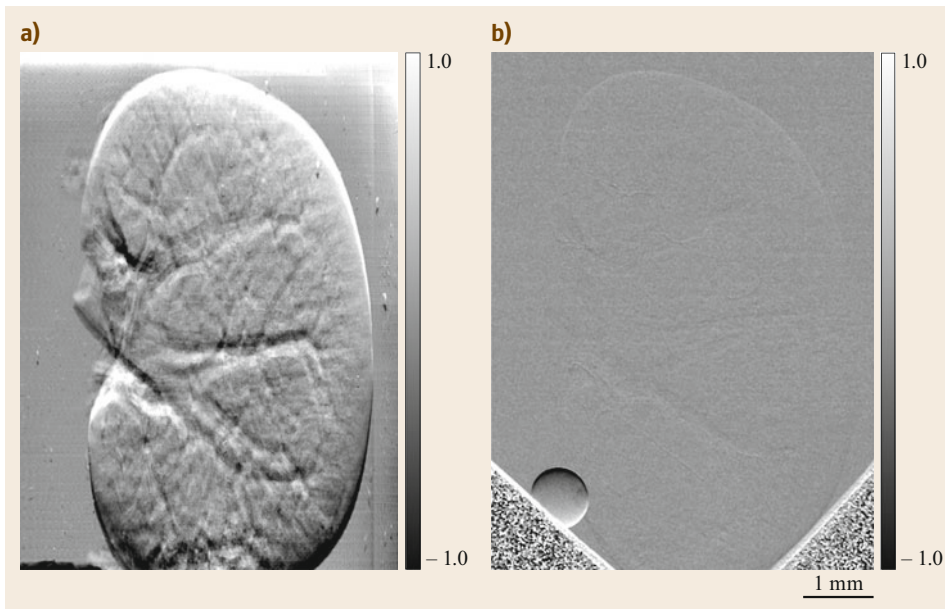


Fig. 30.16a,b Differential phase-contrast images of a formalin-fixed mouse kidney specimen acquired with (a) a grating-Bonse-Hart interferometer consisting of three phase gratings of 200 nm periods, and (b) a Talbot-Lau interferometer consisting of a combination of absorption and phase gratings of 4.8 μm periods. The images are displayed in the same scale, showing an order of magnitude difference in the level of differential phase signal. The branching structures are blood vessels. An air bubble was introduced into the sample vial of the Talbot-Lau interferometer to produce a high phase-contrast signal as a way to verify its correct function

30.7 Conclusion

Projection-based x-ray imaging and microtomography with phase contrast is a continually evolving field where several basic physical concepts have developed into a variety of imaging methods for a wide range of

applications. New imaging physics and technical breakthroughs are being created and the landscape of the field is rapidly shifting with the advances in x-ray sources, detectors and fabrication capabilities of x-ray optics.

References

- | | | | |
|------|---|------|--|
| 30.1 | C.T. Chantler, K. Olsen, R.A. Dragoset, J. Chang, A.R. Kishore, S.A. Kotochigova, D.S. Zucker: <i>X-Ray Form Factor, Attenuation and Scattering Tables</i> , Version 2.1 (NIST, Gaithersburg 2005) | 30.5 | A. Pogany, A.W. Stevenson: Quantitative x-ray projection microscopy: Phase-contrast and multi-spectral imaging, <i>J. Microsc.</i> 207 , 79–96 (2002) |
| 30.2 | A. Snigirev, I. Snigireva, V. Kohn, S. Kuznetsov, I. Schelokov: On the possibilities of x-ray phase contrast microimaging by coherent high-energy synchrotron radiation, <i>Rev. Sci. Instrum.</i> 66 (12), 5486–5492 (1995) | 30.6 | S.C. Mayo, T.J. Davis, T.E. Gureyev, P.R. Miller, D. Paganin, A. Pogany, A.W. Stevenson, S.W. Wilkins: X-ray phase-contrast microscopy and microtomography, <i>Opt. Express</i> 11 (19), 2289–2302 (2003) |
| 30.3 | S.W. Wilkins, T.E. Gureyev, D. Gao, A. Pogany, A.W. Stevenson: Phase-contrast imaging using polychromatic hard x-rays, <i>Nature</i> 384 (6607), 335–338 (1996) | | J. Dudak, J. Zemlicka, J. Karch, M. Patzelt, J. Mrzilkova, P. Zach, Z. Hermanova, J. Kvacek, F. Krejci: High-contrast x-ray micro-radiography and micro-CT of ex-vivo soft tissue murine organs utilizing ethanol fixation and large area photon-counting detector, <i>Sci. Rep.</i> 6 , 30385 (2016) |
| 30.4 | S.C. Mayo, P.R. Miller, S.W. Wilkins, T.J. Davis, D. Gao, T.E. Gureyev, D. Paganin, D.J. Parry, | | |

- 30.7 O. Hemberg, M. Otendal, H.M. Hertz: Liquid-metal-jet anode electron-impact x-ray source, *Appl. Phys. Lett.* **83**(7), 1483–1485 (2003)
- 30.8 D.H. Larsson, U. Lundstrom, U.K. Westermark, M.A. Henriksson, A. Burvall, H.M. Hertz: First application of liquid-metal-jet sources for small-animal imaging: High-resolution CT and phase-contrast tumor demarcation, *Med. Phys.* **40**(2), 021909 (2013)
- 30.9 W. Vagberg, D.H. Larsson, M. Li, A. Arner, H.M. Hertz: X-ray phase-contrast tomography for high-spatial-resolution zebrafish muscle imaging, *Sci. Rep.* **5**, 16625 (2015)
- 30.10 A. Burvall, U. Lundstrom, P.A.C. Takman, D.H. Larsson, H.M. Hertz: Phase retrieval in x-ray phase-contrast imaging suitable for tomography, *Opt. Express* **19**(11), 10359–10376 (2011)
- 30.11 M.A. Beltran, D.M. Paganin, K.K.W. Siu, A. Fouras, S.B. Hooper, D.H. Reser, M.J. Kitchen: Interface-specific x-ray phase retrieval tomography of complex biological organs, *Phys. Med. Biol.* **56**(23), 7353–7369 (2011)
- 30.12 D. Gursoy, M. Das: Single-step absorption and phase retrieval with polychromatic x-rays using a spectral detector, *Opt. Lett.* **38**(9), 1461–1463 (2013)
- 30.13 R.A. Lewis, N. Yagi, M.J. Kitchen, M.J. Morgan, D. Paganin, K.K.W. Siu, K. Pavlov, I. Williams, K. Uesugi, M.J. Wallace, C.J. Hall, J. Whitley, S.B. Hooper: Dynamic imaging of the lungs using x-ray phase contrast, *Phys. Med. Biol.* **50**(21), 5031–5040 (2005)
- 30.14 A.B. Garson, E.W. Izaguirre, S.G. Price, M.A. Anastasio: Characterization of speckle in lung images acquired with a benchtop in-line x-ray phase-contrast system, *Phys. Med. Biol.* **58**(12), 4237–4253 (2013)
- 30.15 R.P. Murrie, K.S. Morgan, A. Maksimenko, A. Fouras, D.M. Paganin, C. Hall, K.K.W. Siu, D.W. Parsons, M. Donnelley: Live small-animal x-ray lung velocimetry and lung micro-tomography at the Australian synchrotron imaging and medical beamline, *J. Synchrotron Radiat.* **22**, 1049–1055 (2015)
- 30.16 M.J. Kitchen, G.A. Buckley, A.F.T. Leong, R.P. Carnibella, A. Fouras, M.J. Wallace, S.B. Hooper: X-ray specks: Low dose in vivo imaging of lung structure and function, *Phys. Med. Biol.* **60**(18), 7259–7276 (2015)
- 30.17 E.H. Kim, M. Preissner, R.P. Carnibella, C.R. Samarage, E. Bennett, M.A. Diniz, A. Fouras, G.R. Zosky, H.D. Jones: Novel analysis of 4-DCT imaging quantifies progressive increases in anatomic dead space during mechanical ventilation in mice, *J. Appl. Physiol.* **123**(3), 578–584 (2017)
- 30.18 C.M. Laperle, T.J. Hamilton, P. Wintermeyer, E. JWalker, D.X. Shi, M.A. Anastasio, Z. Derdak, J.R. Wands, G. Diebold, C. Rose-Petruck: Low density contrast agents for x-ray phase contrast imaging: The use of ambient air for x-ray angiography of excised murine liver tissue, *Phys. Med. Biol.* **53**(23), 6911–6923 (2008)
- 30.19 H. Wen, E.E. Bennett, M.M. Hegedus, S.C. Carroll: Spatial harmonic imaging of x-ray scattering—Initial results, *IEEE Trans. Med. Imaging* **27**(8), 997–1002 (2008)
- 30.20 H. Wen, E.E. Bennett, M.M. Hegedus, S. Rapacchi: Fourier x-ray scattering radiography yields bone structural information, *Radiology* **251**(3), 910–918 (2009)
- 30.21 K.S. Morgan, D.M. Paganin, K.K.W. Siu: Quantitative x-ray phase-contrast imaging using a single grating of comparable pitch to sample feature size, *Opt. Lett.* **36**(1), 55–57 (2011)
- 30.22 K.S. Morgan, D.M. Paganin, K.K.W. Siu: Quantitative single-exposure x-ray phase contrast imaging using a single attenuation grid, *Opt. Express* **19**(20), 19781–19789 (2011)
- 30.23 J. Hartmann: Bemerkungen über den Bau und die Justierung von Spektrographen, *Z. Instrumentenk.* **20**, 47–58 (1900)
- 30.24 Z.F. Huang, K.J. Kang, L. Zhang, Z.Q. Chen, F. Ding, Z.T. Wang, Q.G. Fang: Alternative method for differential phase-contrast imaging with weakly coherent hard x-rays, *Phys. Rev. A* **79**(1), 013815 (2009)
- 30.25 H.H. Wen, E.E. Bennett, R. Kopace, A.F. Stein, V. Pai: Single-shot x-ray differential phase-contrast and diffraction imaging using two-dimensional transmission gratings, *Opt. Lett.* **35**(12), 1932–1934 (2010)
- 30.26 K.S. Morgan, T.C. Petersen, M. Donnelley, N. Farrow, D.W. Parsons, D.M. Paganin: Capturing and visualizing transient x-ray wavefront topological features by single-grid phase imaging, *Opt. Express* **24**(21), 24435–24450 (2016)
- 30.27 W. Yashiro, Y. Terui, K. Kawabata, A. Momose: On the origin of visibility contrast in x-ray Talbot interferometry, *Opt. Express* **18**(16), 16890–16901 (2010)
- 30.28 S.K. Lynch, V. Pai, J. Auxier, A.F. Stein, E.E. Bennett, C.K. Kemble, X.H. Xiao, W.K. Lee, N.Y. Morgan, H.H. Wen: Interpretation of dark-field contrast and particle-size selectivity in grating interferometers, *Appl. Opt.* **50**(22), 4310–4319 (2011)
- 30.29 A.F. Stein, J. Ilavsky, R. Kopace, E.E. Bennett, H. Wen: Selective imaging of nano-particle contrast agents by a single-shot x-ray diffraction technique, *Opt. Express* **18**(12), 13271–13278 (2010)
- 30.30 J.H. Bruning, D.R. Herriott, J.E. Gallagher, D.P. Rosenfeld, A.D. White, D.J. Brangaccio: Digital wavefront measuring interferometer for testing optical surfaces and lenses, *Appl. Opt.* **13**(11), 2693–2703 (1974)
- 30.31 K.J. Harmon, E.E. Bennett, A.A. Gomella, H. Wen: Efficient decoding of 2-D structured illumination with linear phase stepping in x-ray phase contrast and dark-field imaging, *PLoS One* **9**(1), e87127 (2014)
- 30.32 A. Olivo, C.D. Arvanitis, S.E. Bohndiek, A.T. Clark, M. Prydderch, R. Turchetta, R.D. Speller: First evidence of phase-contrast imaging with laboratory

- sources and active pixel sensors, *Nucl. Instrum. Methods Phys. Res. A* **581**(3), 776–782 (2007)
- 30.33 P.R.T. Munro, K. Ignatyev, R.D. Speller, A. Olivo: Phase and absorption retrieval using incoherent x-ray sources, *Proc. Natl. Acad. Sci. U.S.A.* **109**(35), 13922–13927 (2012)
- 30.34 P.C. Diemoz, M. Endrizzi, C.E. Zapata, Z.D. Pešić, C. Rau, A. Bravin, I.K. Robinson, A. Olivo: X-ray phase-contrast imaging with nanoradian angular resolution, *Phys. Rev. Lett.* **110**(13), 138105 (2013)
- 30.35 H.F. Talbot: LXXVI. Facts relating to optical science, No. IV, *Philos. Mag.* **9**(55), 401–407 (1836)
- 30.36 K.S. Morgan, P. Modregger, S.C. Irvine, S. Rutishauser, V.A. Guzenko, M. Stampanoni, C. David: A sensitive x-ray phase contrast technique for rapid imaging using a single phase grid analyzer, *Opt. Lett.* **38**(22), 4605–4608 (2013)
- 30.37 K.S. Morgan, D.M. Paganin, K.K. Siu: X-ray phase imaging with a paper analyzer, *Appl. Phys. Lett.* **100**(12), 124102 (2012)
- 30.38 S. Berujon, H.C. Wang, I. Pape, K. Sawhney: X-ray phase microscopy using the speckle tracking technique, *Appl. Phys. Lett.* **102**(15), 154105 (2013)
- 30.39 H.C. Wang, Y. Kashyap, K. Sawhney: Speckle based x-ray wavefront sensing with nanoradian angular sensitivity, *Opt. Express* **23**(18), 23310–23317 (2015)
- 30.40 T.H. Zhou, I. Zanette, M.C. Zdora, U. Lundstrom, D.H. Larsson, H.M. Hertz, F. Pfeiffer, A. Burvall: Speckle-based x-ray phase-contrast imaging with a laboratory source and the scanning technique, *Opt. Lett.* **40**(12), 2822–2825 (2015)
- 30.41 E.E. Bennett, R. Kopace, A.F. Stein, H. Wen: A grating-based single-shot x-ray phase contrast and diffraction method for in vivo imaging, *Med. Phys.* **37**(11), 6047–6054 (2010)
- 30.42 D. Rand, V. Ortiz, Y. Liu, Z. Derdak, J.R. Wands, M. Taticek, C. Rose-Petruck: Nanomaterials for x-ray imaging: Gold nanoparticle enhancement of x-ray scatter imaging of hepatocellular carcinoma, *Nano Lett.* **11**(7), 2678–2683 (2011)
- 30.43 D. Rand, M. Uchida, T. Douglas, C. Rose-Petruck: X-ray spatial frequency heterodyne imaging of protein-based nanobubble contrast agents, *Opt. Express* **22**(19), 23290–23298 (2014)
- 30.44 D. Rand, E.G. Walsh, Z. Derdak, J.R. Wands, C. Rose-Petruck: A highly sensitive x-ray imaging modality for hepatocellular carcinoma detection in vitro, *Phys. Med. Biol.* **60**(2), 769–784 (2015)
- 30.45 D. Rand, Z. Derdak, R. Carlson, J.R. Wands, C. Rose-Petruck: X-ray scatter imaging of hepatocellular carcinoma in a mouse model using nanoparticle contrast agents, *Sci. Rep.* **5**, 15673 (2015)
- 30.46 J.F. Clauser, M.W. Reinsch: New theoretical and experimental results in Fresnel optics with applications to matter-wave and x-ray interferometry, *Appl. Phys. B* **54**(5), 380–395 (1992)
- 30.47 P. Cloetens, J.P. Guigay, C. DeMartino, J. Baruchel, M. Schlenker: Fractional Talbot imaging of phase gratings with hard x-rays, *Opt. Lett.* **22**(14), 1059–1061 (1997)
- 30.48 J.F. Clauser: Ultrahigh resolution interferometric x-ray imaging, US Patent 5812629 (1998)
- 30.49 A. Momose, S. Kawamoto, I. Koyama, Y. Hamaishi, K. Takai, Y. Suzuki: Demonstration of x-ray Talbot interferometry, *Jpn. J. Appl. Phys.* **42**(7B), L866–L868 (2003)
- 30.50 T. Weitkamp, A. Diaz, C. David, F. Pfeiffer, M. Stampanoni, P. Cloetens, E. Ziegler: X-ray phase imaging with a grating interferometer, *Opt. Express* **13**(16), 6296–6304 (2005)
- 30.51 F. Pfeiffer, T. Weitkamp, O. Bunk, C. David: Phase retrieval and differential phase-contrast imaging with low-brilliance x-ray sources, *Nat. Phys.* **2**(4), 258–261 (2006)
- 30.52 J. Ming, C.L. Wyatt, G. Wang: X-ray phase-contrast imaging with three 2-D gratings, *J. Biomed. Imaging* **2008**, 827152 (2008)
- 30.53 I. Zanette, T. Weitkamp, T. Donath, S. Rutishauser, C. David: Two-dimensional x-ray grating interferometer, *Phys. Rev. Lett.* **105**(24), 248102 (2010)
- 30.54 S. Marathe, X.B. Shi, M.J. Wojcik, N.G. Kujala, R. Divan, D.C. Mancini, A.T. Macrander, L. Assoufid: Probing transverse coherence of x-ray beam with 2-D phase grating interferometer, *Opt. Express* **22**(12), 14041–14053 (2014)
- 30.55 P. Modregger, S. Rutishauser, J. Meiser, C. David, M. Stampanoni: Two-dimensional ultra-small angle x-ray scattering with grating interferometry, *Appl. Phys. Lett.* **105**(2), 024102 (2014)
- 30.56 A. Momose, W. Yashiro, H. Kuwabara, K. Kawabata: Grating-based x-ray phase imaging using multiline x-ray source, *Jpn. J. Appl. Phys.* **48**(7), 076512 (2009)
- 30.57 Y. Du, X. Liu, Y.H. Lei, J.C. Guo, H.B. Niu: Non-absorption grating approach for x-ray phase contrast imaging, *Opt. Express* **19**(23), 22669–22674 (2011)
- 30.58 Y.H. Lei, X. Liu, J.C. Guo, Z.G. Zhao, H.B. Niu: Development of x-ray scintillator functioning also as an analyser grating used in grating-based x-ray differential phase contrast imaging, *Chin. Phys. B* **20**(4), 042901 (2011)
- 30.59 S. Rutishauser, I. Zanette, T. Donath, A. Sahlholm, J. Linnros, C. David: Structured scintillator for hard x-ray grating interferometry, *Appl. Phys. Lett.* **98**(17), 171107 (2011)
- 30.60 Y.S. Ge, K. Li, J. Garrett, G.H. Chen: Grating based x-ray differential phase contrast imaging without mechanical phase stepping, *Opt. Express* **22**(12), 14246–14252 (2014)
- 30.61 A. Momose: Demonstration of phase-contrast x-ray computed tomography using an x-ray interferometer, *Nucl. Instrum. Methods Phys. Res. A* **352**(3), 622–628 (1995)
- 30.62 I. Zanette, M. Bech, A. Rack, G. Le Duc, P. Tafforeau, C. David, J. Mohr, F. Pfeiffer, T. Weitkamp: Trimodal low-dose x-ray tomography, *Proc. Natl. Acad. Sci. U.S.A.* **109**(26), 10199–10204 (2012)
- 30.63 H. Miao, L. Chen, E.E. Bennett, N.M. Adamo, A.A. Gomella, A.M. Deluca, A. Patel, N.Y. Morgan, H. Wen: Motionless phase stepping in x-ray phase

- contrast imaging with a compact source, Proc. Natl. Acad. Sci. U.S.A. **110**(48), 19268–19272 (2013)
- 30.64 T. Koehler, H. Daerr, G. Martens, N. Kuhn, S. Loscher, U. van Stevendaal, E. Roessl: Slit-scanning differential x-ray phase-contrast mammography: Proof of concept experimental studies, Med. Phys. **42**(4), 1959–1965 (2015)
- 30.65 S. Bachche, M. Nonoguchi, K. Kato, M. Kageyama, T. Koike, M. Kuribayashi, A. Momose: X-ray phase scanning setup for non-destructive testing using Talbot–Lau interferometer, Proc. SPIE **9964**, 99640F (2016)
- 30.66 H. Wen, H. Miao, E.E. Bennett, N.M. Adamo, L. Chen: Flexible retrospective phase stepping in x-ray scatter correction and phase contrast imaging using structured illumination, PLoS One **8**(10), e78276 (2013)
- 30.67 D. Stutman, M. Finkenthal, N. Moldovan: Development of microperiodic mirrors for hard x-ray phase-contrast imaging, Appl. Opt. **49**(25), 4677–4686 (2010)
- 30.68 H. Wen, C.K. Kemble, E.E. Bennett: Theory of oblique and grazing incidence Talbot–Lau interferometers and demonstration in a compact source x-ray reflective interferometer, Opt. Express **19**(25), 25093–25112 (2011)
- 30.69 M. Hoshino, K. Uesugi, N. Yagi: Phase-contrast x-ray microtomography of mouse fetus, Biol. Open **1**, 269–274 (2012)
- 30.70 A. Sarapata, J.W. Stayman, M. Finkenthal, J.H. Siewerdsen, F. Pfeiffer, D. Stutman: High energy x-ray phase contrast CT using glancing-angle grating interferometers, Med. Phys. **41**(2), 021904 (2014)
- 30.71 H. Miao, A. Panna, A.A. Gomella, E.E. Bennett, S. Znati, L. Chen, H. Wen: A universal moiré effect and application in x-ray phase-contrast imaging, Nat. Phys. **12**(9), 830–834 (2016)
- 30.72 H. Miao, A.A. Gomella, N. Chedid, L. Chen, H. Wen: Fabrication of 200 nm period hard x-ray phase gratings, Nano Lett. **14**(6), 3453–3458 (2014)
- 30.73 D.A. Pushin, M.G. Huber, D.S. Hussey, D.L. Jacobson, J.M. La Manna, H. Miao, D. Sarenac, H. Wen: Phase-grating interferometer for thermal and cold neutrons. In: *8th Am. Conf. Neutron Scatt., Long Beach* (2016)
- 30.74 M. Kagias, Z. Wang, K. Jefimovs, M. Stampanoni: Dual phase grating interferometer for tunable dark-field sensitivity, Appl. Phys. Lett. **110**(1), 014105 (2017)
- 30.75 J.M. Cowley, A.F. Moodie: Fourier images the phase grating, Proc. Phys. Soc. **76**(489), 378–384 (1960)
- 30.76 H. Miao, A.A. Gomella, K.J. Harmon, E.E. Bennett, N. Chedid, S. Znati, A. Panna, B.A. Foster, P. Bhandarkar, H. Wen: Enhancing tabletop x-ray phase contrast imaging with nano-fabrication, Sci. Rep. **5**, 13581 (2015)
- 30.77 G. Schulz, C. Waschkies, F. Pfeiffer, I. Zanette, T. Weitkamp, C. David, B. Müller: Multimodal imaging of human cerebellum—Merging x-ray phase microtomography, magnetic resonance microscopy and histology, Sci. Rep. **2**, 826 (2012)
- 30.78 M. Stampanoni, Z.T. Wang, T. Thuring, C. David, E. Roessl, M. Trippel, R.A. Kubik–Huch, G. Singer, M.K. Hohl, N. Hauser: The first analysis and clinical evaluation of native breast tissue using differential phase-contrast mammography, Invest. Radiol. **46**(12), 801–806 (2011)
- 30.79 S. Schleede, M. Bech, S. Grandl, A. Sztrokay, J. Herzen, D. Mayr, M. Stockmar, G. Potdevin, I. Zanette, A. Rack, T. Weitkamp, F. Pfeiffer: X-ray phase-contrast tomosynthesis for improved breast tissue discrimination, Eur. J. Radiol. **83**(3), 531–536 (2014)
- 30.80 T. Michel, J. Rieger, G. Anton, F. Bayer, M.W. Beckmann, J. Durst, P.A. Fasching, W. Haas, A. Hartmann, G. Pelzer, M. Radicke, C. Rauh, A. Ritter, P. Sievers, R. Schulz–Wendtland, M. Uder, D.L. Wachter, T. Weber, E. Wenkel, A. Zang: On a dark-field signal generated by micrometer-sized calcifications in phase-contrast mammography, Phys. Med. Biol. **58**(8), 2713–2732 (2013)
- 30.81 G. Anton, F. Bayer, M.W. Beckmann, J. Durst, P.A. Fasching, W. Haas, A. Hartmann, T. Michel, G. Pelzer, M. Radicke, C. Rauh, J. Rieger, A. Ritter, R. Schulz–Wendtland, M. Uder, D.L. Wachter, T. Weber, E. Wenkel, L. Wucherer: Grating-based darkfield imaging of human breast tissue, Z. Med. Phys. **23**(3), 228–235 (2013)
- 30.82 S. Schleede, F.G. Meinel, M. Bech, J. Herzen, K. Achterhold, G. Potdevin, A. Malecki, S. Adam-Neumair, S.F. Thieme, F. Bamberg, K. Nikolaou, A. Bohla, A.O. Yildirim, R. Loewen, M. Gifford, R. Ruth, O. Eickelberg, M. Reiser, F. Pfeiffer: Emphysema diagnosis using x-ray dark-field imaging at a laser-driven compact synchrotron light source, Proc. Natl. Acad. Sci. U.S.A. **109**(44), 17880–17885 (2012)
- 30.83 A. Yaroshenko, F.G. Meinel, M. Bech, A. Tapfer, A. Velroyen, S. Schleede, S. Auweter, A. Bohla, A.O. Yildirim, K. Nikolaou, F. Bamberg, O. Eickelberg, M.F. Reiser, F. Pfeiffer: Pulmonary emphysema diagnosis with a preclinical small-animal x-ray dark-field scatter-contrast scanner, Radiology **269**(2), 426–432 (2013)
- 30.84 K. Hellbach, A. Yaroshenko, F.G. Meinel, A.O. Yildirim, T.M. Conlon, M. Bech, M. Mueller, A. Velroyen, M. Notohamiprodjo, F. Bamberg, S. Auweter, M. Reiser, O. Eickelberg, F. Pfeiffer: In vivo dark-field radiography for early diagnosis and staging of pulmonary emphysema, Invest. Radiol. **50**(7), 430–435 (2015)
- 30.85 M. Uehara, W. Yashiro, A. Momose: Effectiveness of x-ray grating interferometry for non-destructive inspection of packaged devices, J. Appl. Phys. **114**(13), 134901 (2013)
- 30.86 M.S. Nielsen, L.B. Christensen, R. Feidenhansl: Frozen and defrosted fruit revealed with x-ray dark-field radiography, Food Control **39**, 222–226 (2014)
- 30.87 M.P. Valdivia, D. Stutman, M. Finkenthal: Single-shot Z_{eff} dense plasma diagnostic through

- simultaneous refraction and attenuation measurements with a Talbot-Lau x-ray moiré deflector, *Appl. Opt.* **54**(10), 2577–2583 (2015)
- 30.88 A. Tapfer, M. Bech, B. Pauwels, X. Liu, P. Bruyn-donckx, A. Sasov, J. Kenntner, J. Mohr, M. Walter, J. Schulz, F. Pfeiffer: Development of a prototype gantry system for preclinical x-ray phase-contrast computed tomography, *Med. Phys.* **38**(11), 5910–5915 (2011)
- 30.89 A. Momose, W. Yashiro, K. Kido, J. Kiyohara, C. Makifuchi, T. Ito, S. Nagatsuka, C. Honda, D. Noda, T. Hattori, T. Endo, M. Nagashima, J. Tanaka: X-ray phase imaging: From synchrotron to hospital, *Philos. Trans. R. Soc. A* **372**, 20130023 (2010)
- 30.90 T.J. Davis, D. Gao, T.E. Gureyev, A.W. Stevenson, S.W. Wilkins: Phase-contrast imaging of weakly absorbing materials using hard x-rays, *Nature* **373**(6515), 595–598 (1995)
- 30.91 D. Chapman, W. Thomlinson, R.E. Johnston, D. Washburn, E. Pisano, N. Gmur, Z. Zhong, R. Menk, F. Arfelli, D. Sayers: Diffraction enhanced x-ray imaging, *Phys. Med. Biol.* **42**(11), 2015–2025 (1997)
- 30.92 Z. Zhong, W. Thomlinson, D. Chapman, D. Sayers: Implementation of diffraction-enhanced imaging experiments: At the NSLS and APS, *Nucl. Instrum. Methods Phys. Res. A* **450**(2/3), 556–567 (2000)
- 30.93 E.D. Pisano, R.E. Johnston, D. Chapman, J. Geradts, M.V. Iacocca, C.A. Livasy, D.B. Washburn, D.E. Sayers, Z. Zhong, M.Z. Kiss, W.C. Thomlinson: Human breast cancer specimens: Diffraction-enhanced imaging with histologic correlation—Improved conspicuity of lesion detail compared with digital radiography, *Radiology* **214**(3), 895–901 (2000)
- 30.94 B.W. Batterman, H. Cole: Dynamical diffraction of x-rays by perfect crystals, *Rev. Mod. Phys.* **36**(3), 681–717 (1964)
- 30.95 E. Pagot, P. Cloetens, S. Fiedler, A. Bravin, P. Coan, J. Baruchel, J. Hartwig, W. Thomlinson: A method to extract quantitative information in analyzer-based x-ray phase contrast imaging, *Appl. Phys. Lett.* **82**(20), 3421–3423 (2003)
- 30.96 C. Parham, Z. Zhong, D.M. Connor, L.D. Chapman, E.D. Pisano: Design and implementation of a compact low-dose diffraction enhanced medical imaging system, *Acad. Radiol.* **16**(8), 911–917 (2009)
- 30.97 I. Nesch, D.P. Fogarty, T. Tzvetkov, B. Reinhardt, A.C. Walus, G. Khelashvili, C. Muehleman, D. Chapman: The design and application of an in-laboratory diffraction-enhanced x-ray imaging instrument, *Rev. Sci. Instrum.* **80**(9), 093702 (2009)
- 30.98 M. Ando, N. Sunaguchi, Y.L. Wu, S. Do, Y.J. Sung, A. Louissaint, T. Yuasa, S. Ichihara, R. Gupta: Crystal analyser-based x-ray phase contrast imaging in the dark field: Implementation and evaluation using excised tissue specimens, *Eur. Radiol.* **24**(2), 423–433 (2014)
- 30.99 S. Gasilov, A. Mittone, E. Brun, A. Bravin, S. Grandl, P. Coan: On the possibility of quantitative refractive-index tomography of large biomedical samples with hard x-rays, *Biomed. Opt. Express* **4**(9), 1512–1518 (2013)
- 30.100 M.O. Hasnah, Z. Zhong, O. Oltulu, E.D. Pisano, R.E. Johnston, D. Sayers, W. Thomlinson, D. Chapman: Diffraction enhanced imaging contrast mechanisms in breast cancer specimens, *Med. Phys.* **29**(10), 2216–2221 (2002)
- 30.101 M. Fernandez, J. Keyrilainen, R. Serimaa, M. Torkkeli, M.L. Karjalainen-Lindsberg, M. Leidenius, K. von Smitten, M. Tenhunen, S. Fiedler, A. Bravin, T.M. Weiss, P. Suortti: Human breast cancer in vitro: Matching histo-pathology with small-angle x-ray scattering and diffraction enhanced x-ray imaging, *Phys. Med. Biol.* **50**(13), 2991–3006 (2005)
- 30.102 L. Faulconer, C. Parham, D.M. Connor, Z. Zhong, E. Kim, D.L. Zeng, C. Livasy, E. Cole, C. Kuzmiak, M. Koomen, D. Pavic, E. Pisano: Radiologist evaluation of an x-ray tube-based diffraction-enhanced imaging prototype using full-thickness breast specimens, *Acad. Radiol.* **16**(11), 1329–1337 (2009)
- 30.103 T. Kao, D. Connor, F.A. Dilmanian, L. Faulconer, T. Liu, C. Parham, E.D. Pisano, Z. Zhong: Characterization of diffraction-enhanced imaging contrast in breast cancer, *Phys. Med. Biol.* **54**(10), 3247–3256 (2009)
- 30.104 Y.Z. Zhao, E. Brun, P. Coan, Z.F. Huang, A. Sztrokay, P.C. Diemoz, S. Liebhart, A. Mittone, S. Gasilov, J.W. Miao, A. Bravin: High-resolution, low-dose phase contrast x-ray tomography for 3-D diagnosis of human breast cancers, *Proc. Natl. Acad. Sci. U.S.A.* **109**(45), 18290–18294 (2012)
- 30.105 C. Muehleman, J. Li, Z. Zhong, J.G. Brankov, M.N. Wernick: Multiple-image radiography for human soft tissue, *J. Anat.* **208**(1), 115–124 (2006)
- 30.106 C. Muehleman, J. Li, D. Connor, C. Parham, E. Pisano, Z. Zhong: Diffraction-enhanced imaging of musculoskeletal tissues using a conventional x-ray tube, *Acad. Radiol.* **16**(8), 918–923 (2009)
- 30.107 M.N. Wernick, O. Wirjadi, D. Chapman, Z. Zhong, N.P. Galatsanos, Y.Y. Yang, J.G. Brankov, O. Oltulu, M.A. Anastasio, C. Muehleman: Multiple-image radiography, *Phys. Med. Biol.* **48**(23), 3875–3895 (2003)
- 30.108 J. Li, Z. Zhong, R. Lidtke, K.E. Kuettner, C. Penterfer, E. Aliyeva, C. Muehleman: Radiography of soft tissue of the foot and ankle with diffraction enhanced imaging, *J. Anat.* **202**(5), 463–470 (2003)
- 30.109 R.A. Lewis, C.J. Hall, A.P. Hufton, S. Evans, R.H. Menk, F. Arfelli, L. Rigon, G. Tromba, D.R. Dance, I.O. Ellis, A. Evans, E. Jacobs, S.E. Pinder, K.D. Rogers: X-ray refraction effects: Application to the imaging of biological tissues, *Br. J. Radiol.* **76**(905), 301–308 (2003)
- 30.110 N. Zhu, D. Chapman, D. Cooper, D.J. Schreyer, X.B. Chen: X-ray diffraction enhanced imaging as

- a novel method to visualize low-density scaffolds in soft tissue engineering, *Tissue Eng. C* **17**(11), 1071–1080 (2011)
- 30.111 Z. Izadifar, A. Honaramooz, S. Wiebe, G. Belev, X.B. Chen, D. Chapman: Low-dose phase-based x-ray imaging techniques for in situ soft tissue engineering assessments, *Biomaterials* **82**, 151–167 (2016)
- 30.112 U. Bonse, M. Hart: An x-ray interferometer, *Appl. Phys. Lett.* **6**(8), 155–156 (1965)
- 30.113 U. Bonse, M. Hart: Moiré patterns of atomic planes obtained by x-ray interferometry, *Z. Phys.* **190**(4), 455–467 (1966)
- 30.114 L. Zehnder: Ein neuer Interferenzrefraktor, *Z. Instrum.* **11**, 275–285 (1891)
- 30.115 A. Momose, A. Fukuda: Phase-contrast radiographs of nonstained rat cerebellar specimen, *Med. Phys.* **22**(4), 375–379 (1995)
- 30.116 F. Beckmann, U. Bonse, F. Busch, O. Gunnewig: X-ray microtomography (μ CT) using phase contrast for the investigation of organic matter, *J. Comput. Assist. Tomogr.* **21**(4), 539–553 (1997)
- 30.117 A. Yoneyama, T. Takeda, Y. Tsuchiya, J. Wu, T.L. Thet, A. Koizumi, K. Hyodo, Y. Itai: A phase-contrast x-ray imaging system—with a 60 × 30 mm field of view—based on a skew-symmetric two-crystal x-ray interferometer, *Nucl. Instrum. Methods Phys. Res. A* **523**(1/2), 217–222 (2004)
- 30.118 T. Takeda, A. Yoneyama, J. Wu, T.L. Thet, A. Momose, K. Hyodo: In vivo physiological saline-infused hepatic vessel imaging using a two-crystal-interferometer-based phase-contrast x-ray technique, *J. Synchrotron Radiat.* **19**, 252–256 (2012)
- 30.119 A. Momose, T. Takeda, Y. Itai, K. Hirano: Phase-contrast x-ray computed tomography for observing biological soft tissues, *Nat. Med.* **2**(4), 473–475 (1996)
- 30.120 C. David, B. Nohammer, H.H. Solak, E. Ziegler: Differential x-ray phase contrast imaging using a shearing interferometer, *Appl. Phys. Lett.* **81**(17), 3287–3289 (2002)
- 30.121 H. Wen, A.A. Gomella, A. Patel, S.K. Lynch, N.Y. Morgan, S.A. Anderson, E.E. Bennett, X. Xiao, C. Liu, D.E. Wolfe: Subnanoradian x-ray phase-contrast imaging using a far-field interferometer of nanometric phase gratings, *Nat. Commun.* **4**, 2659 (2013)
- 30.122 H. Wen, A.A. Gomella, A. Patel, D.E. Wolfe, S.K. Lynch, X. Xiao, N.Y. Morgan: Boosting phase contrast with a grating Bonse–Hart interferometer of 200 nanometre grating period, *Philos. Trans. R. Soc. A* **372**(2010), 20130028 (2014)



Han Wen

National Heart, Lung and Blood Institute
National Institutes of Health
Bethesda, MD, USA
han.wen@nih.gov

Han Wen received his PhD from the University of Maryland, College Park. He works at the US National Institutes of Health, where he has been the Principal Investigator of the Imaging Physics Laboratory, National Heart, Lung, and Blood Institute since 1997. He has worked in the areas of magnetic resonance imaging, ultrasound imaging and x-ray imaging.